Supporting Information

Micropore-Confined P/O-Codoped Carbon Cages Stabilize Molybdenum Single-Atom Sites for Sulfur Conversion in Aluminum-Sulfur Batteries

Su Yang[1,2, †], Xiaolu Ma[2, †], Qian Bai[2], Runmin Li[2], Rui Yang[2], Jilin Li[2], Zhengbang Zhu[2], Weng-Chon (Max) Cheong[4], Wenxing Chen[2, *], Handong Jiao[1, *], Shuqiang Jiao[3, *]

[1] Institute of Advanced Structure Technology, Beijing Institute of Technology, Beijing, P R China

[2] Energy & Catalysis Center, School of Materials Science and Engineering, Beijing Institute of Technology, Beijing 100081 China.

[3] State Key Laboratory of Advanced Metallurgy, University of Science and Technology Beijing, Beijing, PR China

[4] Sino–Luso Joint Laboratory for Optoelectronics, Macao Institute of Materials Science and Engineering (MIMSE), Macau University of Science and Technology, Macao SAR 999078, China

* Correspondence to: wxchen@bit.edu.cn (W.C.); jiaohandong_new@163.com (H.J.); sjiao@ustb.edu.cn (S.J.)

† These authors contributed equally to this work.

Section 1. Experimental and Characterization Details

Preparation of the Mo-SA@P,O-PC/S Composite

Sulfur was loaded by melt diffusion. Mo-SA@P,O-PC and sulfur were mixed, sealed, and heated at 155°C for 12h.

A nominal 60 wt% sulfur feed was used for the main composite. Thermogravimetry of Mo-SA@P,O-PC/S was performed under nitrogen using the same nominal 30–600 °C program at 10 K min^{-1}, corresponding to approximately 57.0% total mass loss.

XAFS Data Processing

EXAFS data were processed with Athena and Artemis in the IFEFFIT package.

After post-edge background subtraction and edge-step normalization, chi(k) data were Fourier transformed with a Hanning window to obtain R-space spectra and separate coordination-shell contributions. Quantitative local structural parameters around Mo were obtained by least-squares fitting in Artemis using FEFF8 paths.

EXAFS Fitting Equation

$$\chi(k)=\sum_{j}\frac{N_j S_o^2 F_j(k)}{k R_j^2}\exp[-2k^2\sigma_j^2]\exp[\frac{-2R_j}{\lambda(k)}]\sin[2k R_j+\phi_j(k)]$$

$S0^2$ is the amplitude reduction factor; $F_j(k)$ is the backscattering amplitude; N_j is the coordination number; R_j is the absorber-backscatterer distance; lambda is the mean free path; $phi_{j(k)}$ is the phase shift; and $sigma_j$ is the Debye-Waller factor.

Operando XAFS Measurements

Operando Mo K-edge XAFS was collected at OCP, 1.45 V, and 1.50 V versus Al^{3+}/Al. Energy calibration and data processing followed the ex situ procedure.

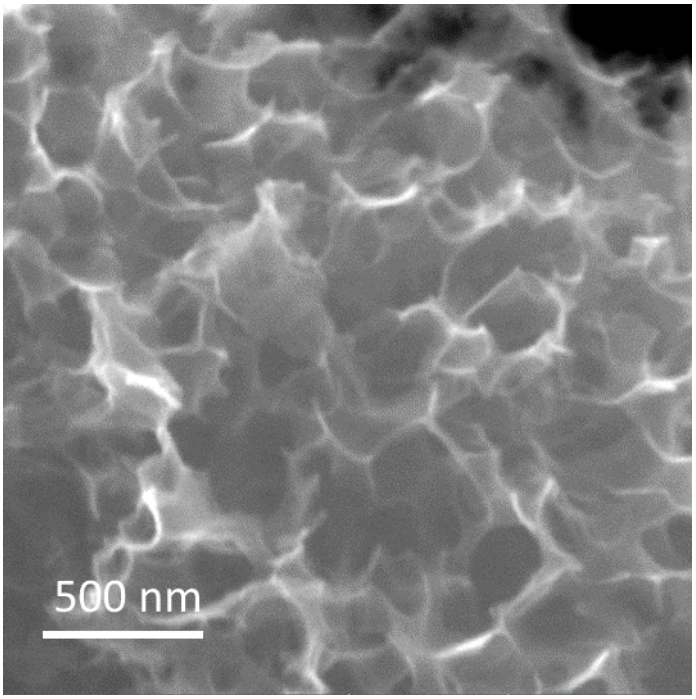


Figure S1. SEM images of micro-PC

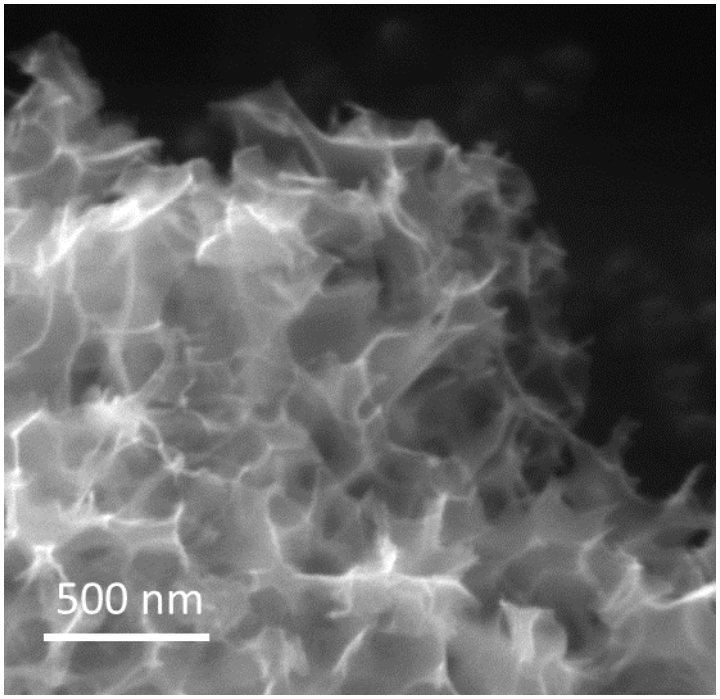


Figure S2. SEM images of POM@micro-PC

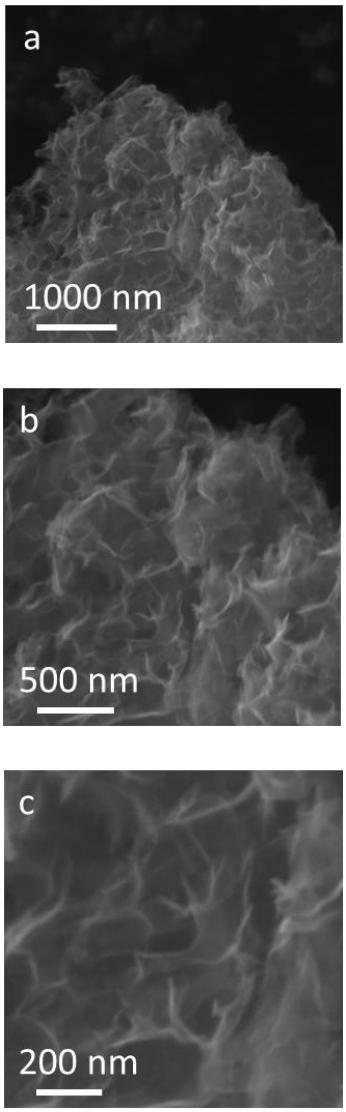


Figure S3. SEM images of Mo-SA@P,O-PC

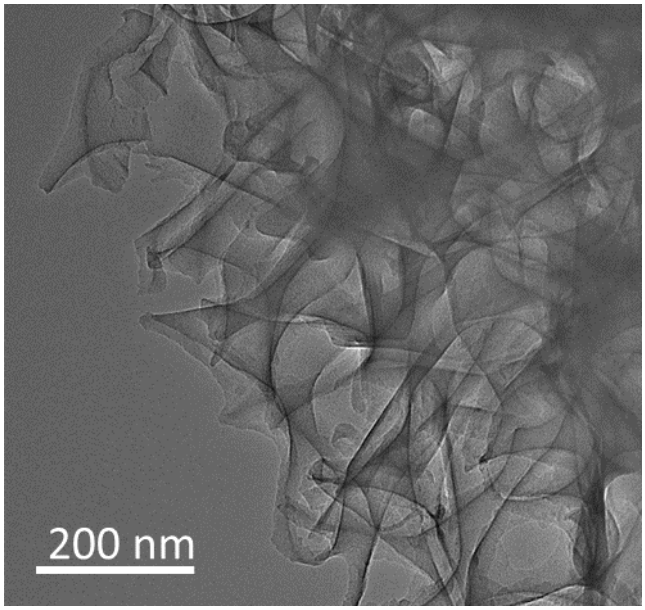


Figure S4. TEM images of PC

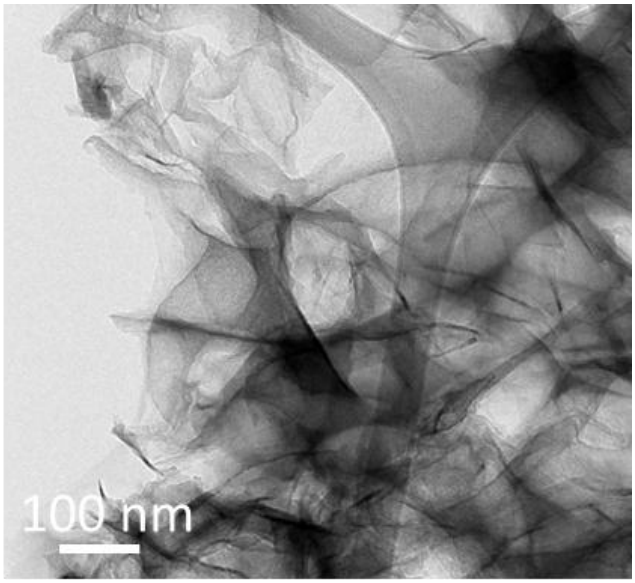


Figure S5. Additional TEM images of PC

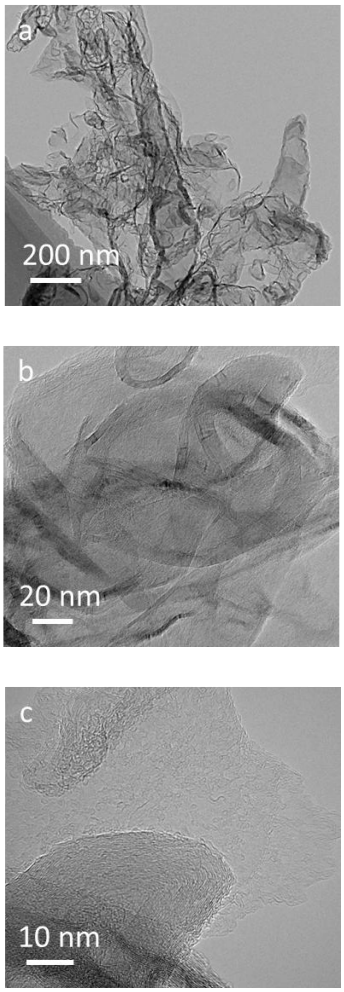


Figure S6. TEM and high-resolution TEM images of Mo-SA@P,O-PC.

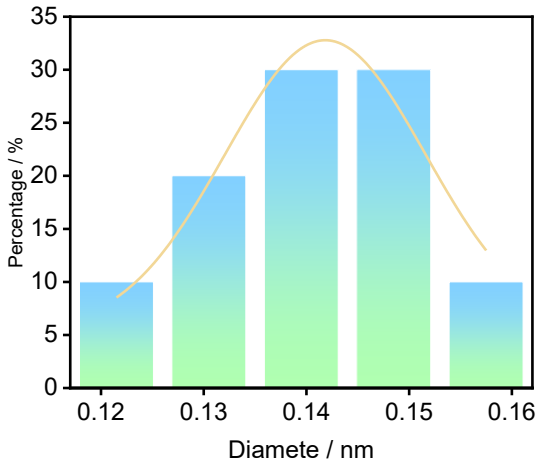


Figure S7. Apparent diameter distribution of isolated high-Z spots in HAADF-STEM images of Mo-SA@P,O-PC. The distribution is centered at approximately 0.14-0.15 nm

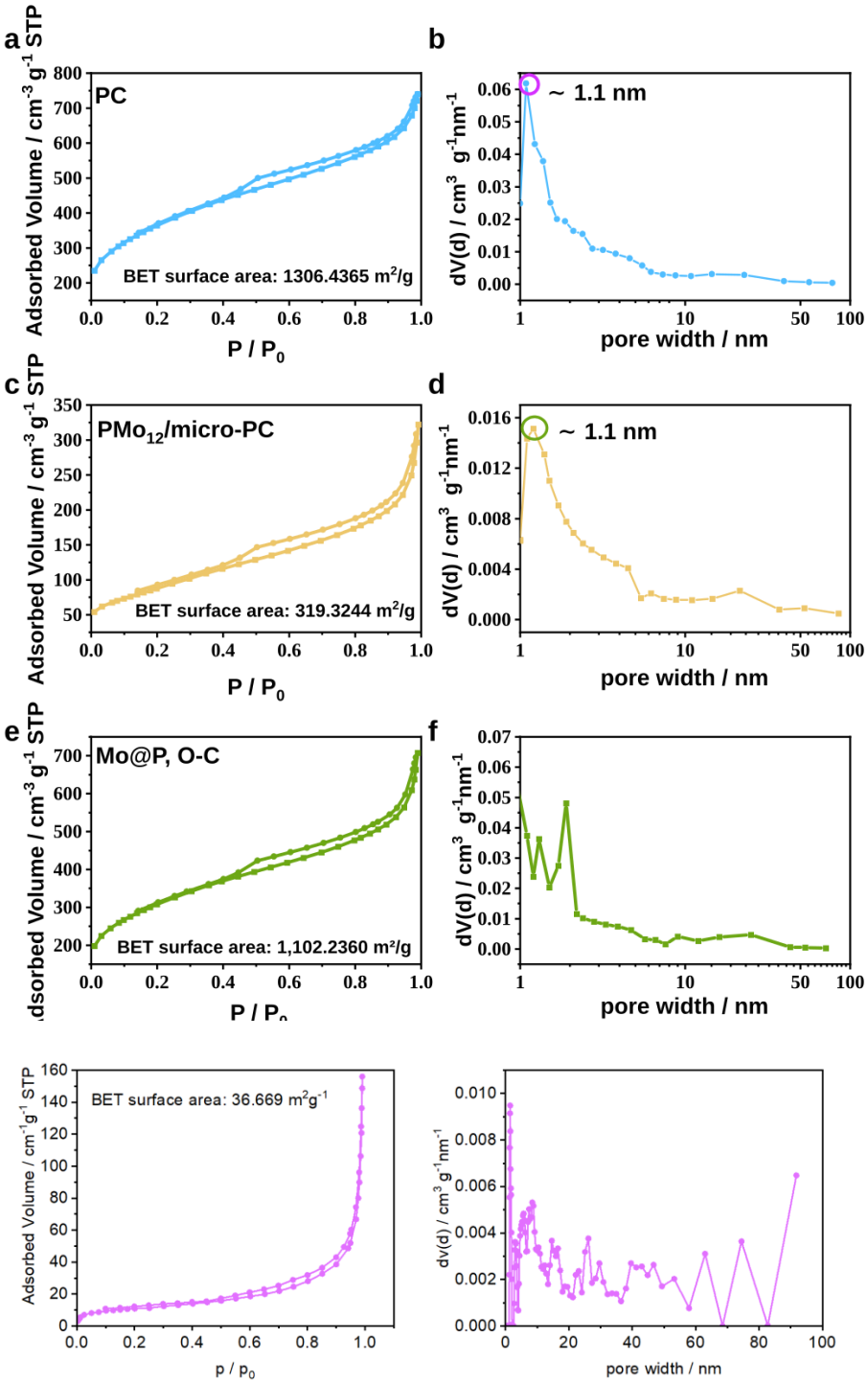


Figure S8. N_2 adsorption-desorption isotherms and pore-size distributions of micro-PC, POM@micro-PC, Mo-SA@P,O-PC and Mo-SA@P,O-PC/S.

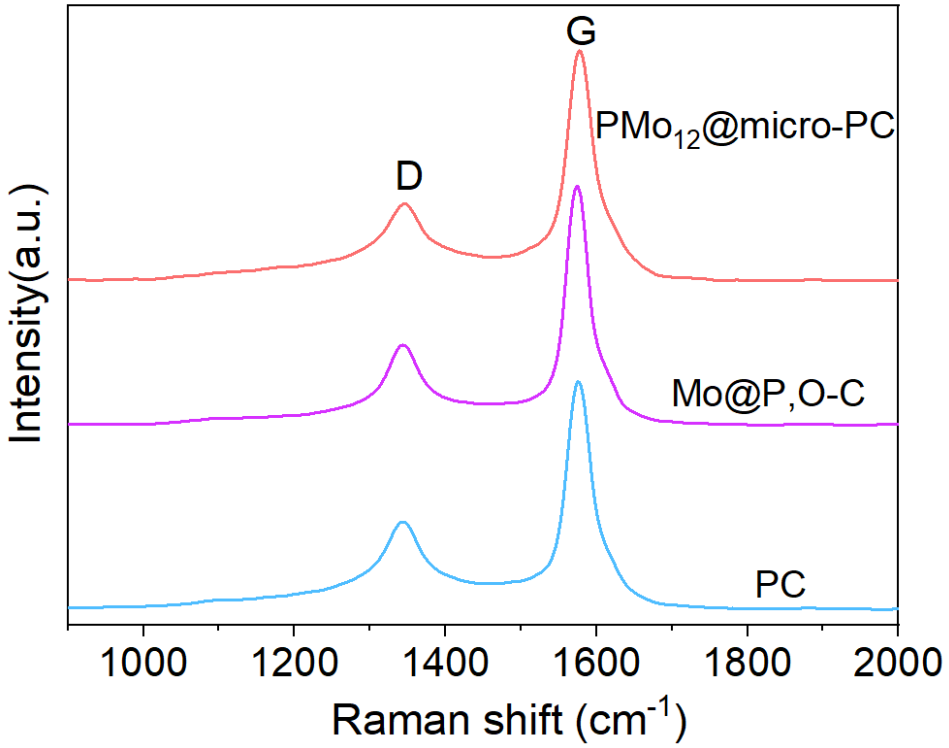


Figure S9. Raman spectra of Mo-SA@P,O-PC, POM@micro-PC, and PC. Relative D/G changes are used to compare defect/edge evolution

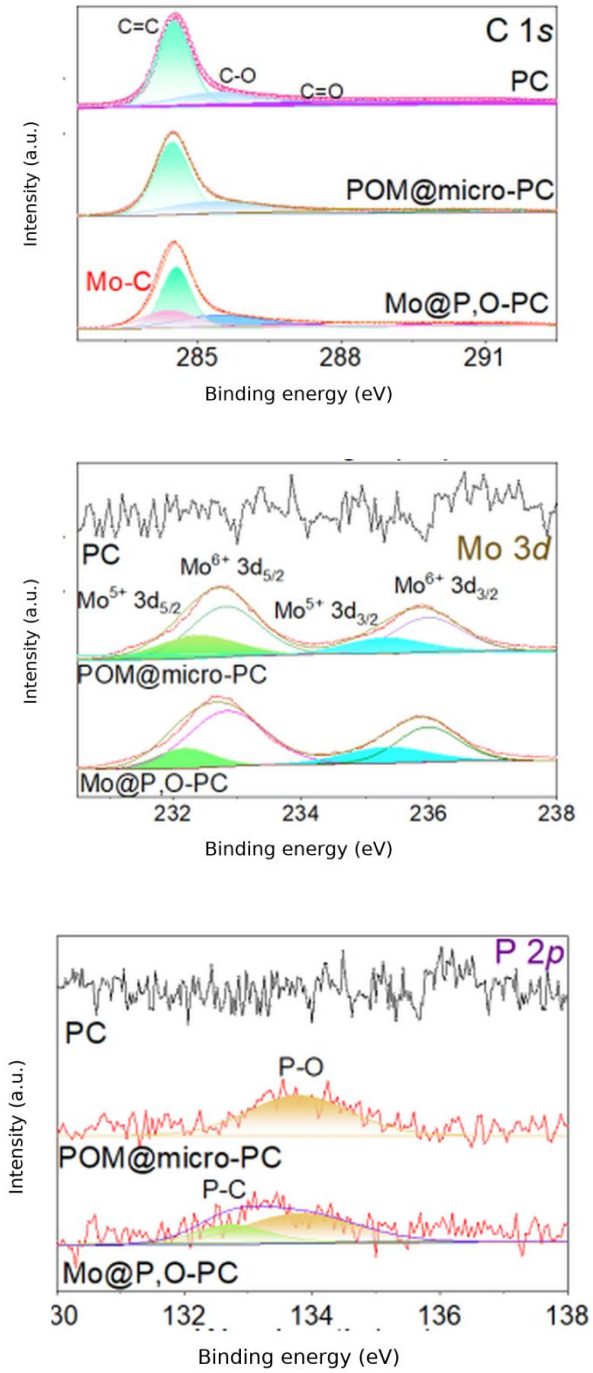


Figure S10. High-resolution XPS spectra plotted as intensity (a.u.) versus binding energy (eV): (a) C 1s, (b) Mo 3d, and (c) P 2p for PC, POM@micro-PC, and Mo-SA@P,O-PC.

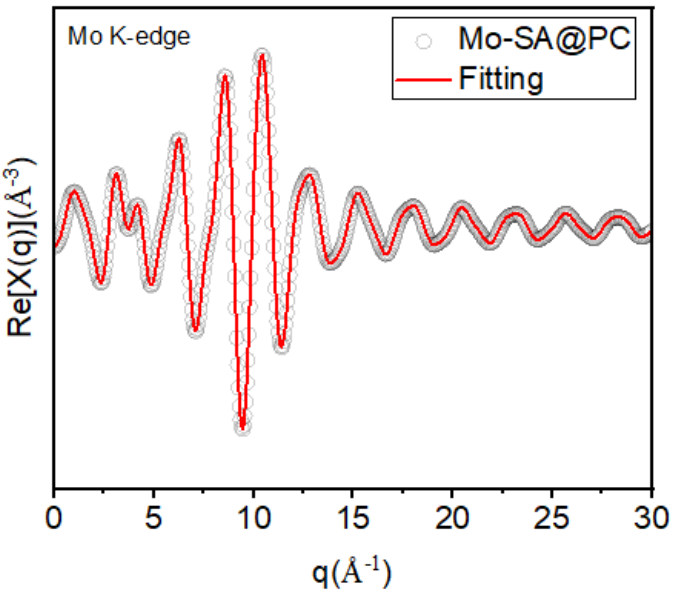


Figure S11. q-space EXAFS fitting curve of Mo-SA@P,O-PC

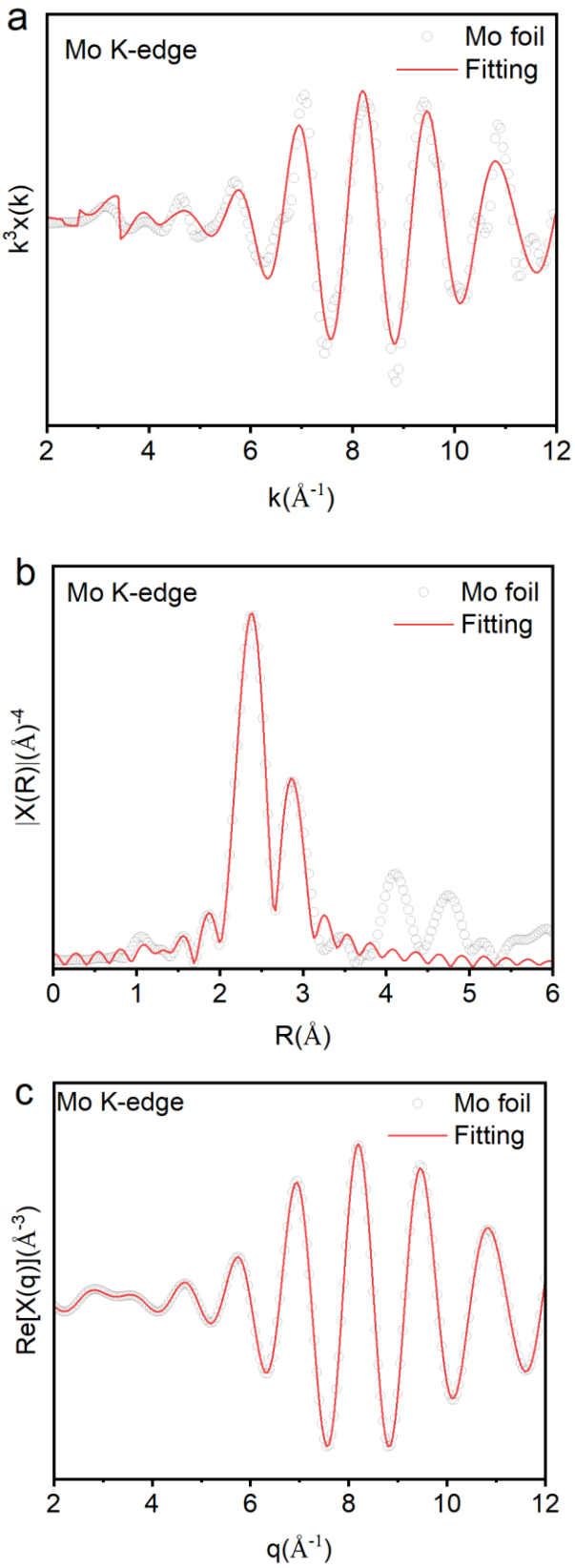


Figure S12. EXAFS fitting curves of Mo foil in (a) k space, (b) R space, and (c) q space

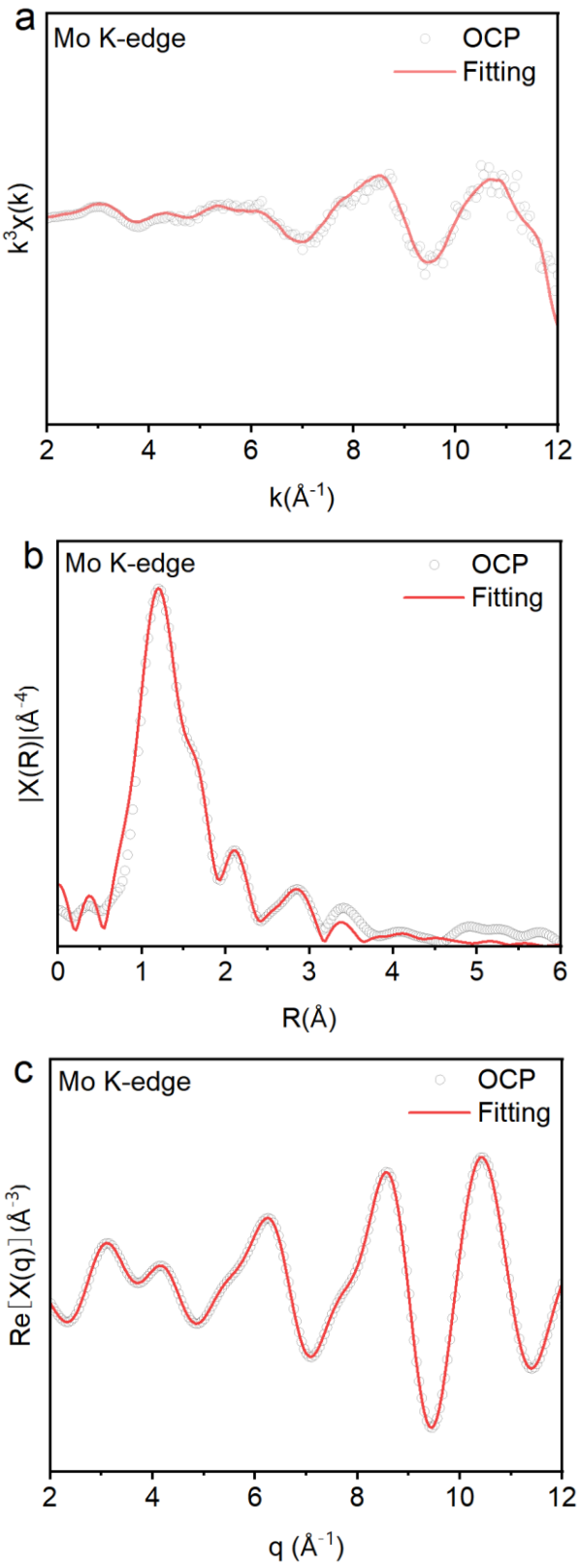


Figure S13. EXAFS fitting curves of Mo-SA@P,O-PC at OCP in (a) k space, (b) R space, and (c) q space.

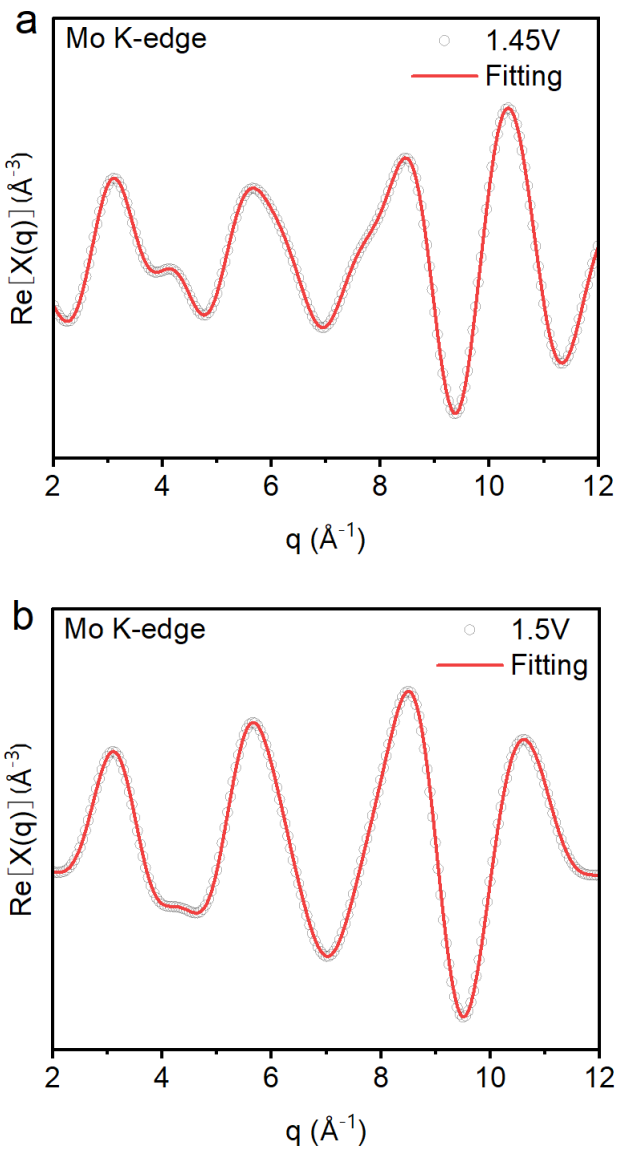


Figure S14. q-space fitting curves of Mo-SA@P,O-PC at 1.45 V and 1.50 V

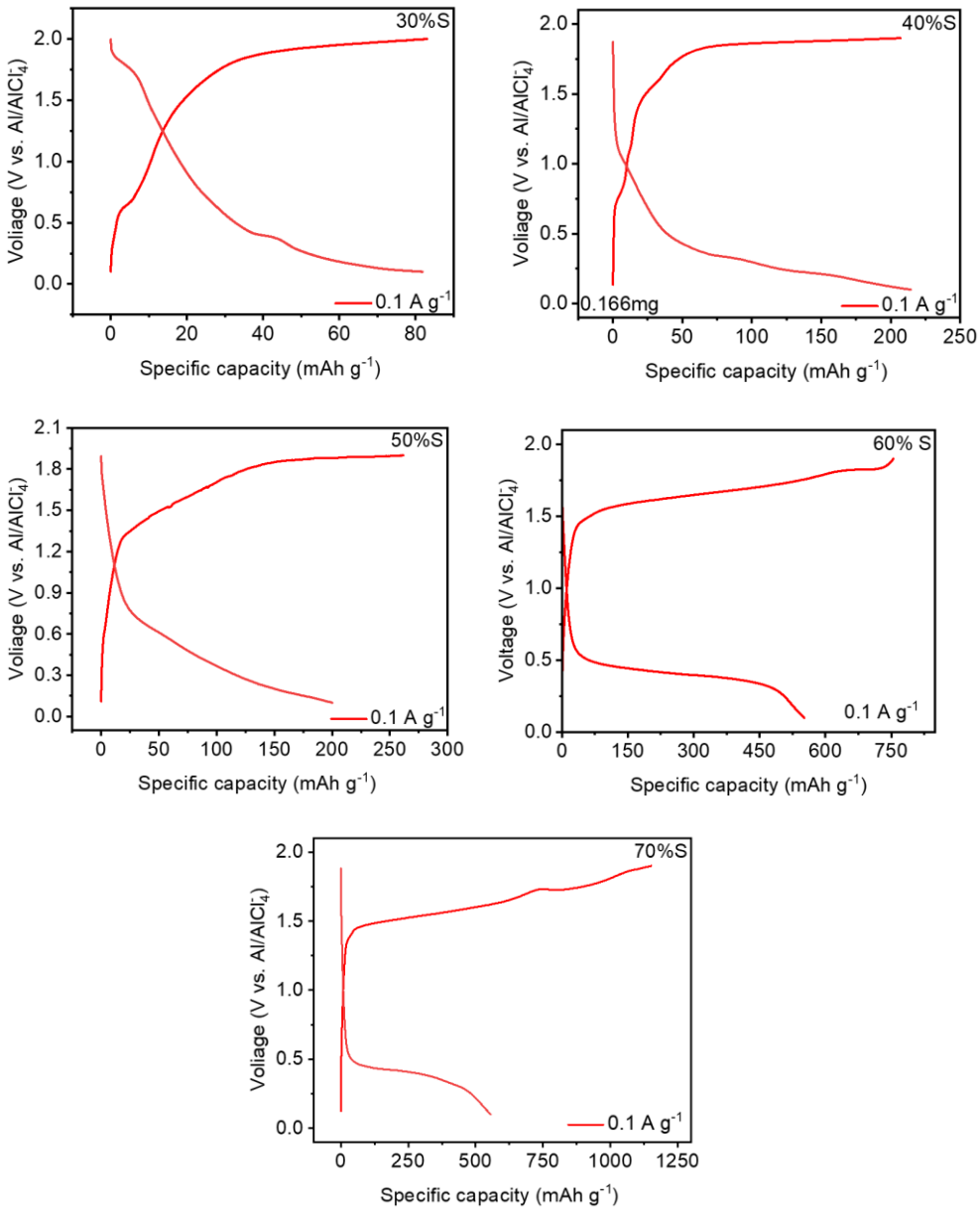


Figure S15. Initial galvanostatic charge-discharge profiles at 0.1 A g^{-1} for Mo-SA@P,O-PC/S electrodes prepared with sulfur feed fractions of 30, 40, 50, 60, and 70 wt%.

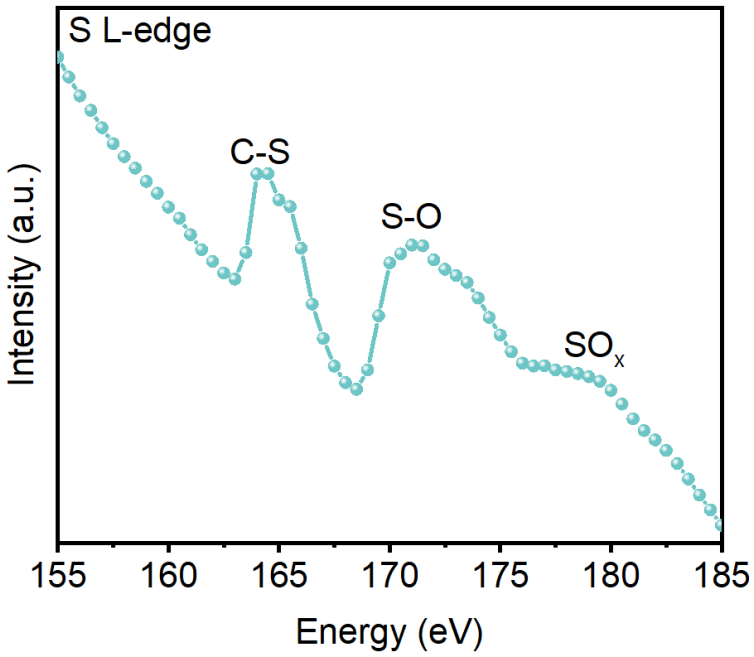


Figure S16. S L-edge XAS spectrum of the sulfur-loaded composite

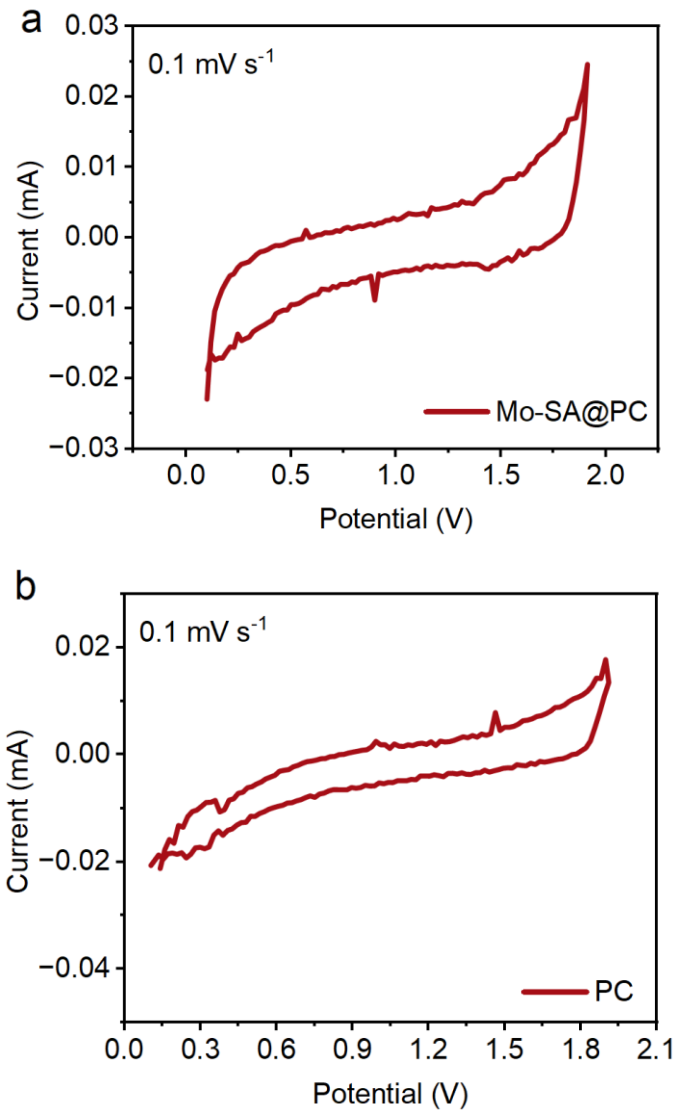


Figure S17. CV curves of (a) sulfur-free Mo-SA@P,O-PC and (b) sulfur-free PC at 0.1 mV s^{-1}.

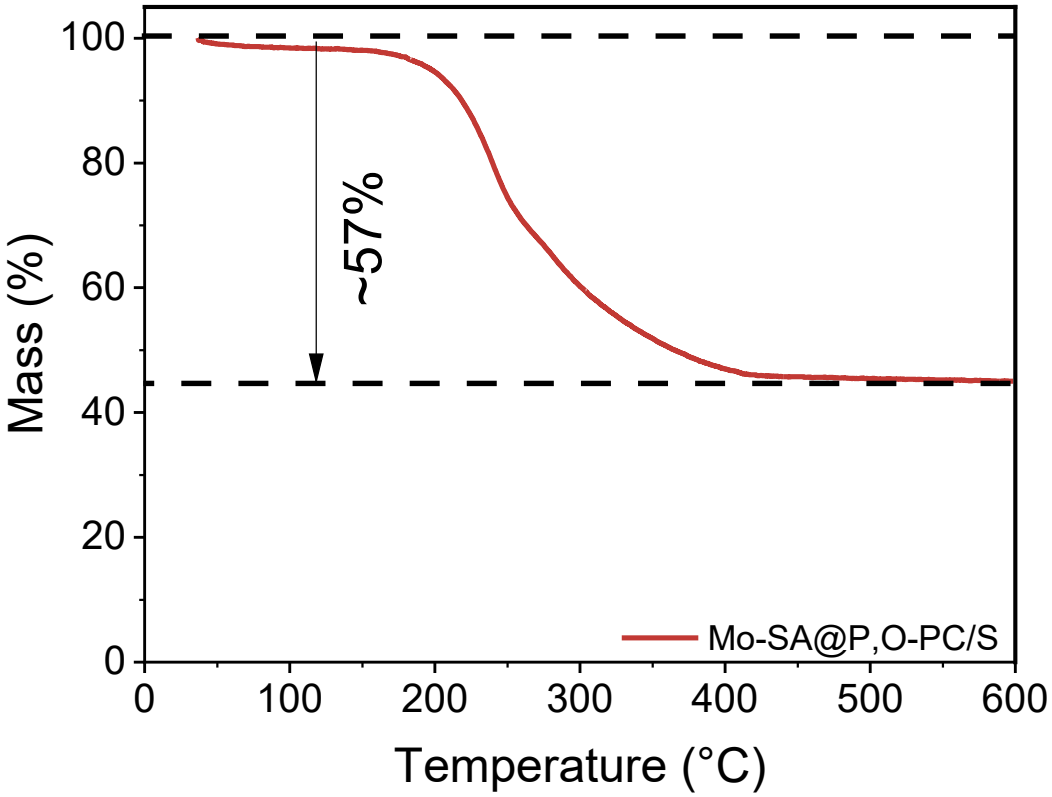


Figure S18. Thermogravimetric curve of Mo-SA@P,O-PC/S acquired under nitrogen at 10 K min^{-1}.

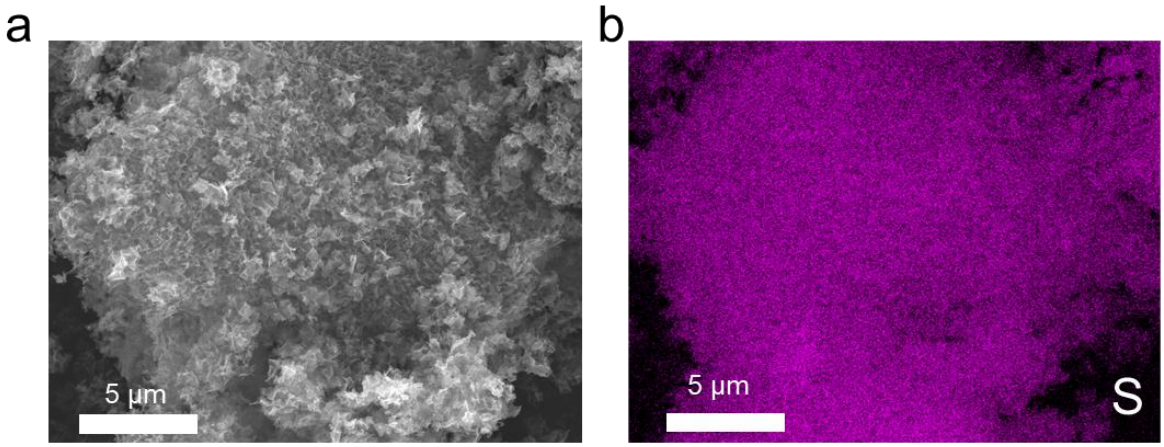


Figure S19. SEM image and corresponding EDS sulfur map of Mo-SA@P,O-PC/S from the same field.

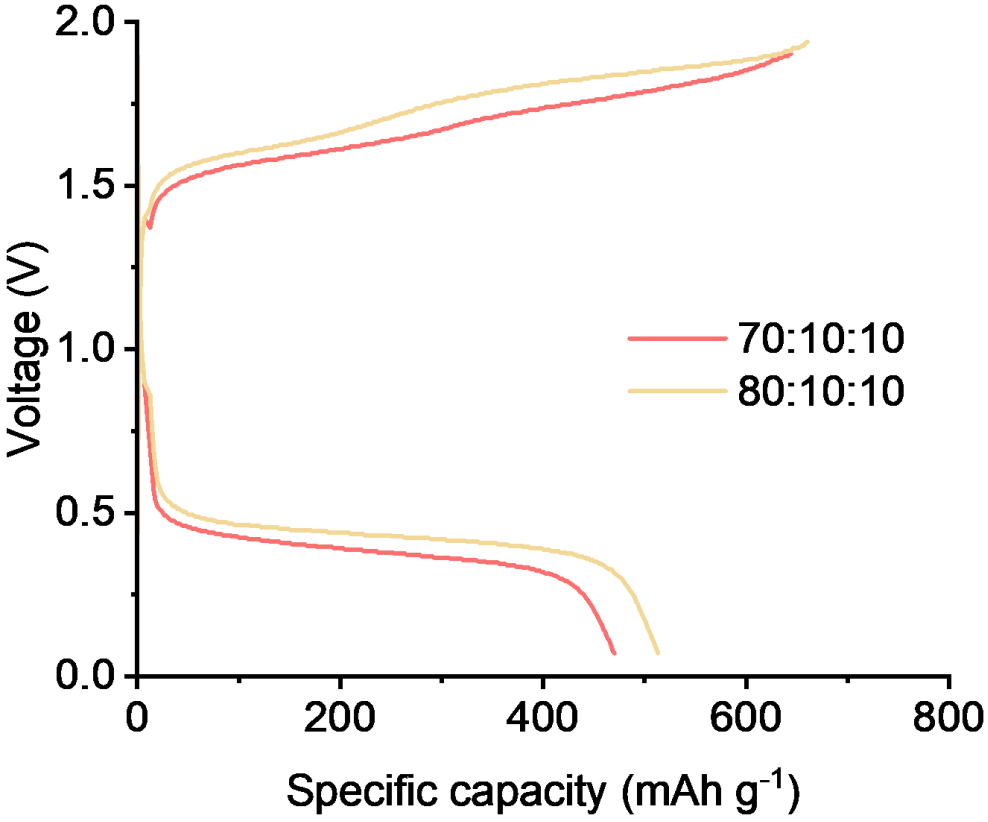


Figure S20. GCD profiles of Mo-SA@P,O-PC/S electrodes with reduced Super P contents.

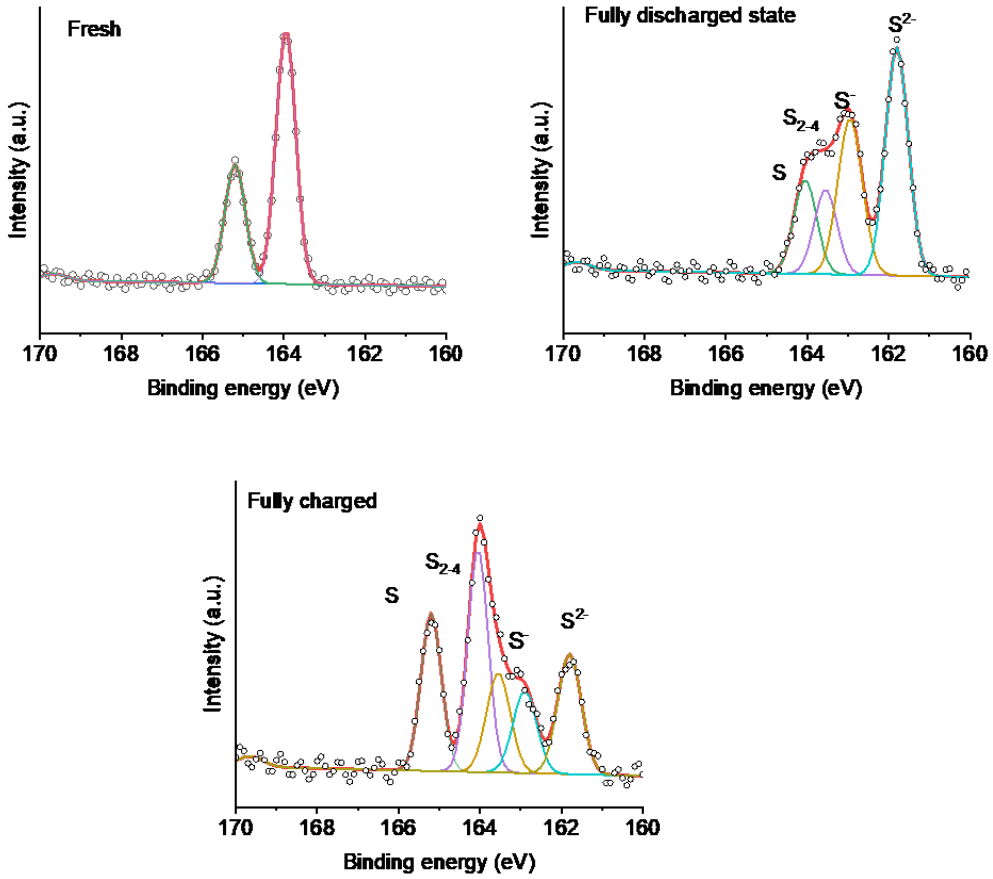


Figure S21. S 2p spectra of fresh, fully discharged, and fully charged electrodes.

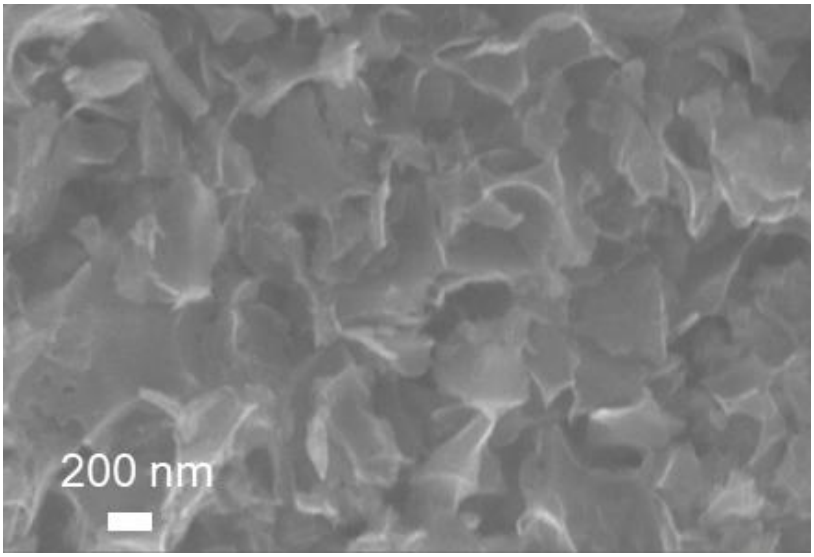


Figure S22. The SEM image of Mo-SA@P,O-PC/S after 200 cycles of circulationM

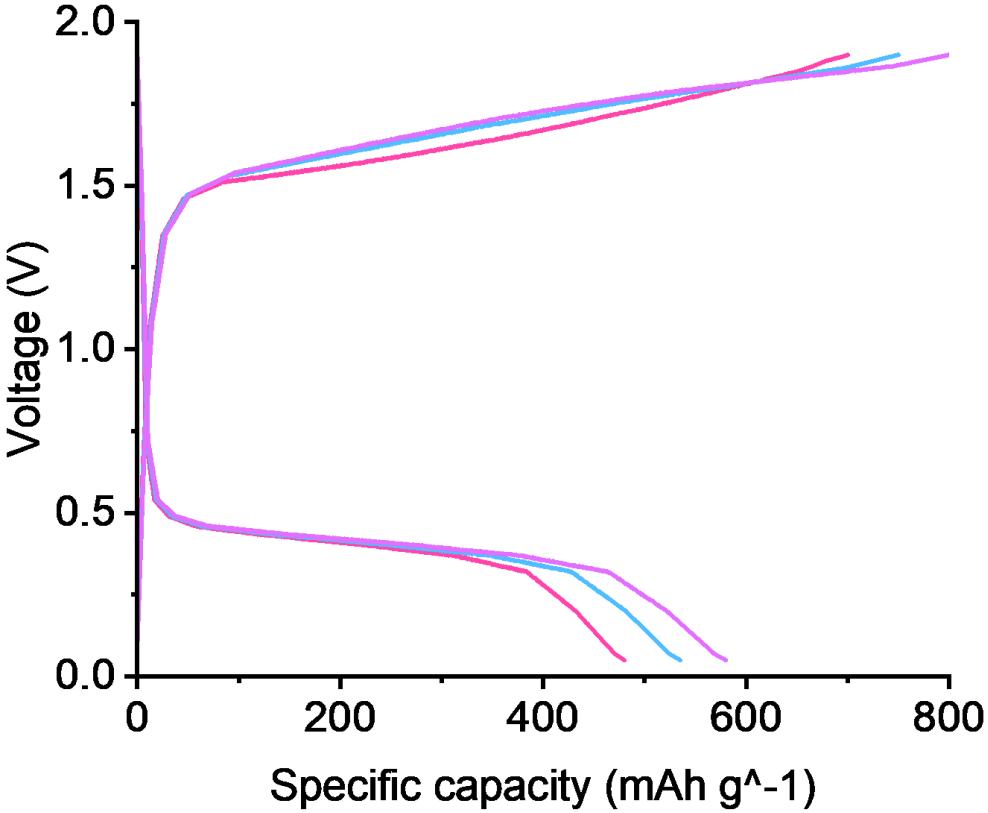


Figure S23. Comparison of three GCD profiles of Mo-SA@P,O-PC/S.

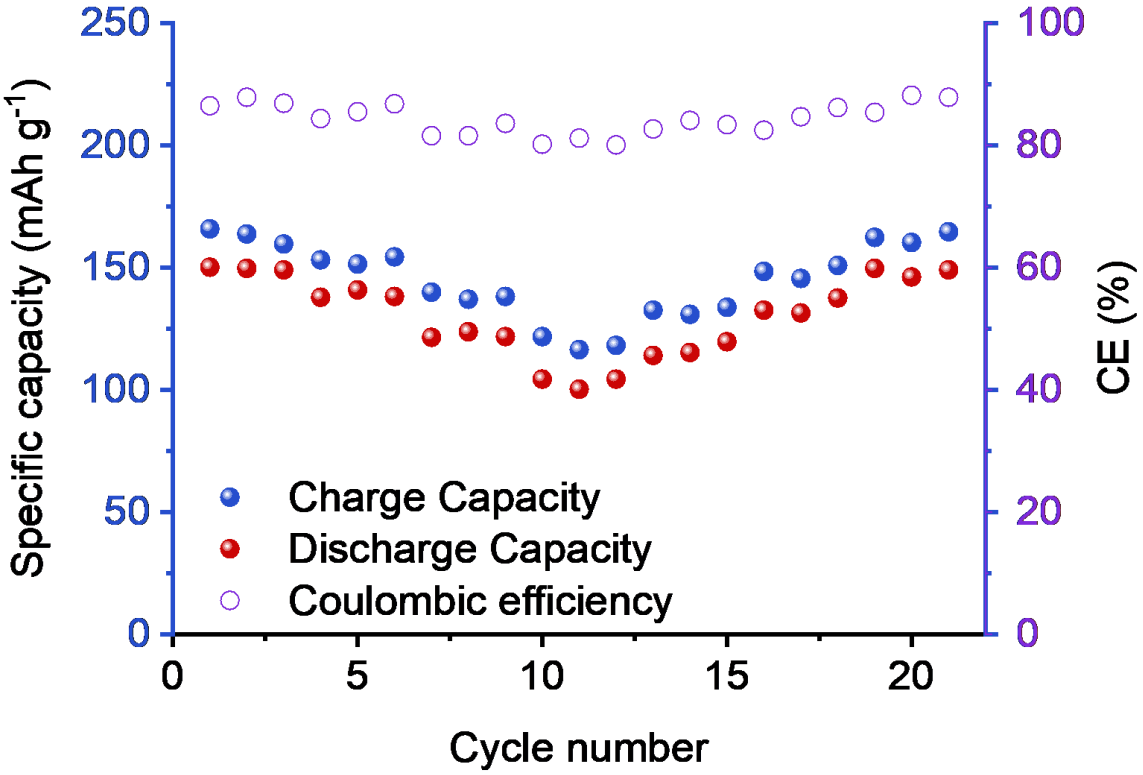


Figure S24. PC/S rate performance at 200, 300, 400, 500, 400, 300, and 200 mA g^{-1}.

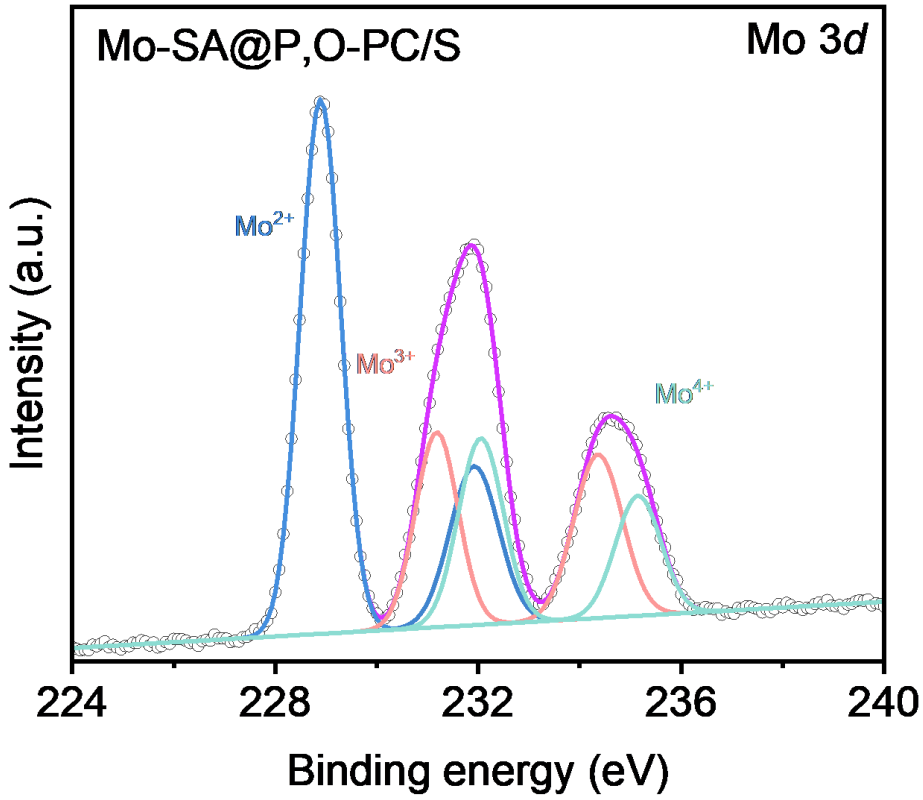


Figure S25. Mo 3d spectra and component peaks of Mo-SA@P,O-PC/S.

Table S1. Elemental composition of the final sulfur-free host.

Element	Content (wt%)	Method and basis
Mo	3.37	ICP; final pyrolyzed, acid-washed, sulfur-free host
P	0.10	ICP; same final host

Table S2. Mo K-edge EXAFS fitting parameters (S_0^2 = 0.84).

Sample	Path	CN	R(Å)	$\sigma^2(10^{-3}Å^2)$	ΔE_0(eV)	R factor
Mo foil	Mo-Mo	8*	2.72±0.01	2.80±0.2	4.3±0.3	0.004
Mo-SA @P,O-PC	Mo-C	3.5±0.5	2.01±0.01	1.98±0.2	5.0±0.1	0.012
	Mo-O	2.2±0.3	2.20±0.02	1.69±0.1	6.3±0.3	0.015

S_0^2: amplitude reduction factor; CN: coordination number; R: absorber–scatterer distance; σ^2: Debye–Waller factor; ΔE_0: edge-energy shift. The R factor measures the goodness of fit. * Fixed during fitting using the known reference structure.

Table S3. Performance comparison of sulfur-containing cathodes for aluminum-based batteries.

Cathodes	Current density ($A\ g^{-1}$)	Cycle number	Capacity ($mAh\ g^{-1}$)	Ref.
Mo-SA@P,O-PC/S	0.10	≈180	140–145	This work
S/CNT	0.20	>200	225	[1]
Ni_3S_2/graphene microflakes	0.20	300	50	[2]
NiS nanobelts	0.20	100	100	[3]
Co_3S_4 microspheres	0.05	150	90	[4]

Table S4. Representative lithium–sulfur catalyst and host designs.

Reference / design	Representative conditions	Reported result
[5] P-Ov-TiO_2-modified PP separator	Pouch cell; 3 mg S cm^{-2}; E/S = 4.5 µL mg S^{-1}; 0.1 C	1004 → 740 mAh g^{-1} after 50 cycles; 73.7% retention
[6] High-index C-Fe_2O_3/rGO separator	9.41 mg S cm^{-2}; 75 µL electrolyte; 0.2 C; 1.7–2.8 V; 1 M LiTFSI in DOL/DME (1:1) with 2% $LiNO_3$	809 mAh g^{-1} (7.61 mAh cm^{-2}) after 85 cycles
[7] BCDs@CNF hosts for both electrodes	Pouch cell; ~8 mg S cm^{-2}; E/S ≈ 2 µL mg S^{-1}; N/P = 2; total sulfur ≈ 1.65 g	~2 Ah; 502 Wh kg^{-1}; 86.4% retention after 10 cycles

Li–S results are listed separately as catalyst-design context; they are not direct performance rankings against Al–S cells.

References

1. Li, H.; Meng, R.; Guo, Y.; et al. Reversible electrochemical oxidation of sulfur in ionic liquid for high-voltage Al−S batteries. *Nat. Commun.* **2021**, *12*, 5714. https://doi.org/10.1038/s41467-021-26056-7.
2. Wang, S.; Yu, Z.; Tu, J.; et al. A Novel Aluminum-Ion Battery: Al/$AlCl_3$-[EMIm]Cl/Ni_3S_2@Graphene. *Adv. Energy Mater.* **2016**, *6*, 1600137. https://doi.org/10.1002/aenm.201600137.
3. Yu, Z.; Kang, Z.; Hu, Z.; et al. Hexagonal NiS nanobelts as advanced cathode materials for rechargeable Al-ion batteries. *Chem. Commun.* **2016**, *52*, 10427–10430. https://doi.org/10.1039/c6cc05974k.
4. Li, H.; Yang, H.; Sun, Z.; et al. A highly reversible Co_3S_4 microsphere cathode material for aluminum-ion batteries. *Nano Energy* **2019**, *56*, 100–108. https://doi.org/10.1016/j.nanoen.2018.11.045.
5. Yang, J.; Jia, X.; Li, B.; et al. Precision-Engineered Nanocatalysts via Lattice Tailoring and d-Band Center Modulation for High-Performance Lithium-Sulfur Batteries. *Carbon Energy* **2025**, *7*, e70043. https://doi.org/10.1002/cey2.70043.
6. Jiang, B.; Tian, D.; Qiu, Y.; et al. High-Index Faceted Nanocrystals as Highly Efficient Bifunctional Electrocatalysts for High-Performance Lithium–Sulfur Batteries. *Nano-Micro Lett.* **2022**, *14*, 40. https://doi.org/10.1007/s40820-021-00769-2.
7. Guo, J.; Liang, H.; Yang, Q.; et al. Steric-Hindrance Effect Induced Fabrication of Lightweight, Bi-Functional, and Easy-to-Infiltrate Hosts for 502 Wh kg^{-1} Lithium-Sulfur Batteries. *Adv. Mater.* **2026**, *38*, e18154. https://doi.org/10.1002/adma.202518154.